APL Materials

Low-damping ferromagnetic resonance in electron-beam patterned, high-Q vanadium tetracyanoethylene magnon cavities

Cite as: APL Mater. **7**, 121113 (2019); https://doi.org/10.1063/1.5131258
Submitted: 10 October 2019 . Accepted: 05 December 2019 . Published Online: 27 December 2019

Andrew Franson, Na Zhu, Seth Kurfman, Michael Chilcote, Denis R. Candido, Kristen S. Buchanan, Michael E. Flatté, Hong X. Tang, and Ezekiel Johnston-Halperin

Low-damping ferromagnetic resonance in electron-beam patterned, high-*Q* vanadium tetracyanoethylene magnon cavities

Cite as: APL Mater. 7, 121113 (2019); doi: 10.1063/1.5131258
Submitted: 10 October 2019 • Accepted: 5 December 2019 •
Published Online: 27 December 2019

Andrew Franson,[1] Na Zhu,[2] Seth Kurfman,[1] Michael Chilcote,[1] Denis R. Candido,[3,4] Kristen S. Buchanan,[5] Michael E. Flatté,[3,4] Hong X. Tang,[2] and Ezekiel Johnston-Halperin[1]

AFFILIATIONS

[1]Department of Physics, The Ohio State University, Columbus, Ohio 43210, USA
[2]Department of Electrical Engineering, Yale University, New Haven, Connecticut 06511, USA
[3]Department of Physics and Astronomy, University of Iowa, Iowa City, Iowa 52242, USA
[4]Pritzker School of Molecular Engineering, University of Chicago, Chicago, Illinois 60637, USA
[5]Department of Physics, Colorado State University, Fort Collins, Colorado 80523, USA

ABSTRACT

Integrating patterned, low-loss magnetic materials into microwave devices and circuits presents many challenges due to the specific conditions that are required to grow ferrite materials, driving the need for flip-chip and other indirect fabrication techniques. The low-loss ($\alpha = (3.98 \pm 0.22) \times 10^{-5}$), room-temperature ferrimagnetic coordination compound vanadium tetracyanoethylene ($V[TCNE]_x$) is a promising new material for these applications that is potentially compatible with semiconductor processing. Here, we present the deposition, patterning, and characterization of $V[TCNE]_x$ thin films with lateral dimensions ranging from 1 μm to several millimeters. We employ electron-beam lithography and liftoff using an aluminum encapsulated poly(methyl methacrylate), poly(methyl methacrylate-methacrylic acid) copolymer bilayer [PMMA/P(MMA-MAA)] on sapphire and silicon. This process can be trivially extended to other common semiconductor substrates. Films patterned via this method maintain low-loss characteristics down to 25 μm with only a factor of 2 increase down to 5 μm. A rich structure of thickness and radially confined spin-wave modes reveals the quality of the patterned films. Further fitting, simulation, and analytic analysis provide an exchange stiffness, $A_{ex} = (2.2 \pm 0.5) \times 10^{-10}$ erg/cm, as well as insights into the mode character and surface-spin pinning. Below a micron, the deposition is nonconformal, which leads to interesting and potentially useful changes in morphology. This work establishes the versatility of $V[TCNE]_x$ for applications requiring highly coherent magnetic excitations ranging from microwave communication to quantum information.

Interest in low-loss magnetic thin films has been growing due to potential applications in magnonics and quantum information as well as the potential for compact, high-efficiency magnetoelectric devices.[1–3] In the field of magnonics and spintronics, yttrium iron garnet ($Y_3Fe_5O_{12}$, YIG), an electrically insulating ferrite that exhibits extremely low Gilbert damping, $\alpha \approx 6 \times 10^{-5}$, and a linewidth of 3.4 G at 9.6 GHz for pristine nanometer-thick films, is currently the leading material for magnetoelectronic circuits.[4,5] The low damping present in YIG films has led to its incorporation in magnetoelectric circuits and its prominent role in magnonics research.[2,6–9] Patterning of YIG, however, presents a challenge. When patterned, the damping increases from $\alpha \approx 4 \times 10^{-4}$ to 8.74×10^{-4} for ion-milled films[10,11] and from $\alpha \approx 2.9 \times 10^{-4}$ to 5×10^{-4} for liftoff-based films.[12–14] Furthermore, postgrowth annealing steps at temperatures as high as 850 °C and deposition on the lattice-matching substrate gadolinium gallium garnet ($Gd_3Ga_5O_{12}$, GGG) are generally required to attain even these degraded damping values, both of which provide strict limits on direct integration with functional devices.[15–17] Vanadium tetracyanoethylene ($V[TCNE]_x$, $x \approx 2$), on the other hand, is a low-loss (sub-Gauss linewidth at 9.83 GHz),

room-temperature (T_c= 600 K) ferrimagnetic semiconductor that can be deposited optimally at 50 °C and 30 mmHg via chemical-vapor deposition (CVD) without the need for lattice matching.[18–20] These relatively benign deposition conditions allow for deposition on a wide variety of substrates and prepatterned circuits, positioning $V[TCNE]_x$ as an exciting option for on-chip magnetic and magnonic device incorporation.[21–23] However, realizing this promise has been limited by the lack of techniques for patterning $V[TCNE]_x$ films at micrometer to submicron length scales.

Here, we present a method for depositing and patterning $V[TCNE]_x$ using standard electron-beam lithography techniques with additional steps to preserve its high T_c and low-loss characteristics. The primary hurdles to micrometer-scale pattering of $V[TCNE]_x$ are its sensitivity to oxygen and solvents traditionally used in fabrication. Our past work has addressed air-sensitivity via encapsulation in a commercial organic light-emitting diode (OLED) epoxy, increasing its lifetime in air from hours to months,[24] and there are other commercial options, such as potting, that promise to protect films indefinitely.[25] This leaves solvent sensitivity that inhibits the use of traditional patterning techniques for two reasons: (i) the presence of solvent in the resist layer inhibits the deposition of $V[TCNE]_x$ as the solvent outgases during growth and (ii) liftoff requires a solvent soak that will, in general, destroy or degrade the CVD-grown $V[TCNE]_x$ film. Here, we address both of these challenges by using a thin AlO_x encapsulating layer for the resist and identifying a $V[TCNE]_x$-compatible solvent, respectively, demonstrating micrometer-scale patterning of $V[TCNE]_x$ films with no apparent increase in microwave loss. The patterned structures are characterized by scanning electron microscopy (SEM) and by a combination of ferromagnetic resonance (FMR) and comparison with micromagnetic simulations and analytic calculations.

The CVD thin-film growth process typically results in a smooth, blue-black $V[TCNE]_x$ film uniformly distributed across the substrate surface. When a resist is applied to the substrate before growth, however, $V[TCNE]_x$ deposition results in nonuniform coverage and poor $V[TCNE]_x$ quality. This is attributed to chemical reactions between the released solvents and the precursors (tetracyanoethylene and vanadium hexacarbonyl). Solvents present in common resists including MICROPOSIT LOR, MICROPOSIT S1800 series, and poly(methyl methacrylate) result in macroscopically inconsistent deposition of $V[TCNE]_x$ across the resist's surface as well as inside patterned areas. In order to address this solvent sensitivity, a 3-nm-thick layer of aluminum is thermally deposited after development to encapsulate the resist layer. The aluminum is then oxidized with a 10-min ultraviolet ozone clean in a UVOCS T10x10/OES prior to $V[TCNE]_x$ deposition.

In prior $V[TCNE]_x$ precipitation synthesis studies, several solvents have been shown to precipitate $V[TCNE]_x$ with a modest impact on the T_c of the resulting powder.[26–28] Since dichloromethane has a small impact on $V[TCNE]_x$ quality and readily dissolves poly(methyl methacrylate) (PMMA) and poly(methyl methacrylate-methacrylic acid 8.5%) [P(MMA 8.5 MAA)] at room temperature, this is the resist-solvent pair chosen to address the challenge of solvent-based liftoff. Specifically, this work focuses on 495PMMA A6 on MMA (8.5) MAA EL 11 as a resist bilayer [PMMA/P(MMA 8.5 MAA)] to additively pattern low-loss $V[TCNE]_x$ onto sapphire, with the understanding that this patterning process should trivially extend to other inorganic substrates.[29,30]

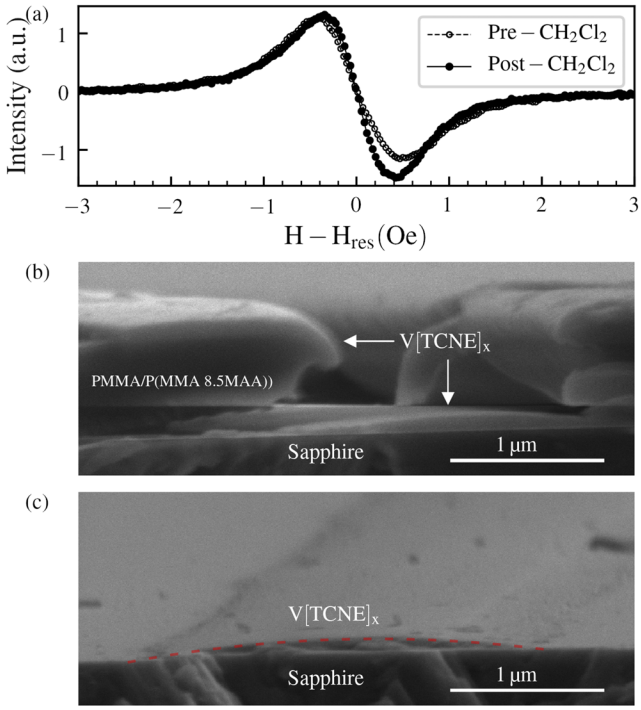

FIG. 1. (a) $V[TCNE]_x$ thin film FMR measured at 9.83 GHz with a resonant field of 3565 Oe before and after a 2.5-h soak in dichloromethane (CH_2Cl_2). SEM images of the patterned $V[TCNE]_x$ film's morphology before (b) and after (c) liftoff with dichloromethane reveal a parabolic deposition morphology into a 2-μm-wide channel. The parabolic cross section is highlighted with a dashed red line in (c).

Figure 1(a) shows the FMR response at 9.83 GHz of a $V[TCNE]_x$ thin film before and after a 2.5-h soak in dichloromethane in a nitrogen atmosphere (<10 ppm 0_2, <2 ppm H_2O). The lineshape of the resonance is largely unchanged. The linewidth narrows slightly, possibly due to changes in the ordering of the $V[TCNE]_x$ due to solvent annealing.[31] The overall similarity indicates little to no incorporation of dichloromethane into the CVD-grown film on that time scale. The $V[TCNE]_x$ growth morphology that results from the above process is characterized by SEM and is shown in Figs. 1(b) and 1(c). Unlike physical vapor deposition, CVD is driven by a combination of flow and diffusion. Figure 1(b) shows how the $V[TCNE]_x$ deposition is limited by the flow characteristics through the patterned features. In particular, $V[TCNE]_x$ does not form vertical sidewalls but rather forms gently sloped sidewalls at an angle of about 6° over a distance of approximately a micrometer from the edge. This leads to a parabolic profile, as one would expect from the velocity profile resulting from laminar flow through a channel [Fig. 1(c)]. These results suggest that there are likely opportunities to tune the structure profile by controlling the channel width, flow direction, resist height, and resist morphology. This cross-sectional profile is difficult to achieve with other material systems and deposition techniques,[32] and it may prove beneficial for studies of spin-wave confinement as it offers a means to realize an approximation of an adiabatic boundary.

Flow-limited deposition can, in principle, also lead to anisotropy in patterned features based on alignment between the flow direction and internal structure. Figure 2 shows the absence and presence of growth anisotropy in various patterned structures of V[TCNE]$_x$ that are designed to explore these effects. The deposition time for these samples is 1.0 h, leading to a nominal thickness of 300 nm. All shapes in Fig. 2 have a faint outline that reveals the ballistically deposited AlO_x layer. In Figs. 2(g)–2(j), dashed black curves have been superimposed over the AlO_x outline to make it easier to compare the AlO_x and V[TCNE]$_x$ morphology. The outlines show

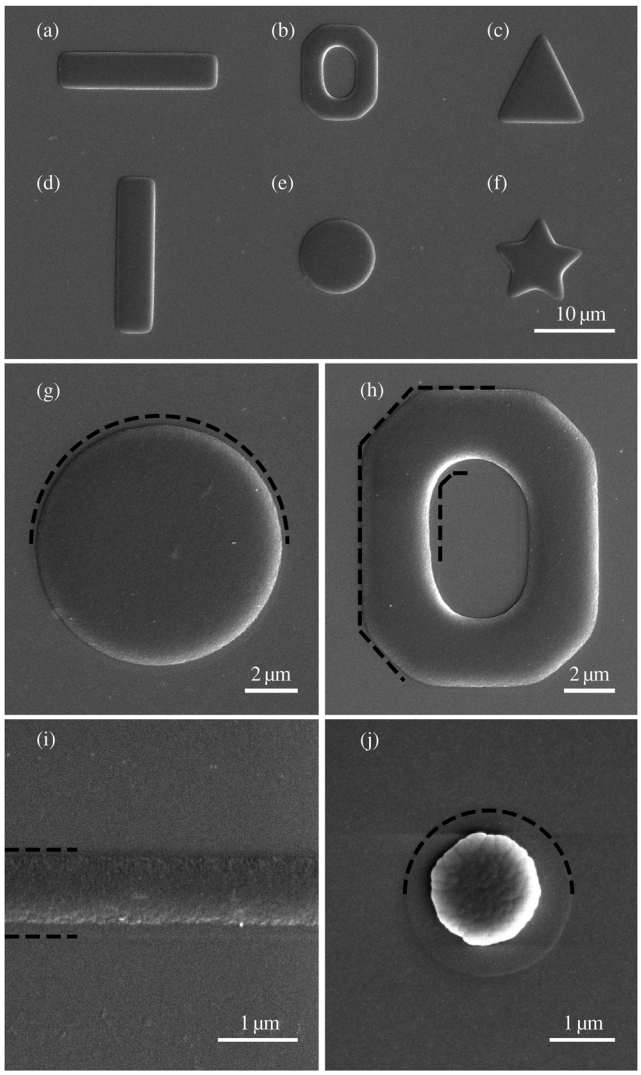

FIG. 2. Top view SEM images of various V[TCNE]$_x$ patterns after a 1.0-hour growth, about 300 nm thick. (a)–(f) Deposition morphology of several shapes with various features ranging from concave to convex to antidot. (g) and (h) Enhanced views of (e) and (b), respectively, show that flow-induced anisotropy is present in the complex block O shape (h). (i) and (j) For features of order 1 μm or smaller, the restricted flow begins to affect the pattern deposition. The dashed black curves in (g)–(j) highlight the AlO_x profile that is present for all shapes.

that there is little to no offset or ellipticity present in the patterned 10-μm-diameter V[TCNE]$_x$ disk. Figure 2(h), however, shows significant anisotropy as measured by the differences between the AlO_x outline and the V[TCNE]$_x$ pattern. The flow direction across the shape is left to right with a 20° tilt toward the top. The flow direction manifests in a more complete, laminar profile along the top and bottom, whereas eddies inhibit deposition in the left and right interior edges. For laminar flow over a step edge, these eddies are predicted to have a width comparable to the height of the step (in this case, the thickness of the PMMA/MMA bilayer).[33,34] This is consistent with the fact that the 540-nm-thick PMMA/P[MMA 8.5 MAA)] bilayer results in a roughly 500-nm-wide region of reduced flow which leads to a taper in the morphology. This effect is also seen in Figs. 2(c)and 2(f) where the concave features at the corners see a reduction in deposition roughly 800 nm away from the planned shape shown by each AlO_x peak.

Figures 2(i) and 2(j) further explore the impacts of length scale on gas flow and the growth morphology using bars and disks. The 1-μm-wide bar in Fig. 2(i) acts as a channel for gas flow, yielding a parabolic deposition profile similar to Figs. 1(b) and 1(c) across the shape and good filling of the ballistic profile when the thickness of the bar in Fig. 2(i) is about 200 nm. In contrast, the 1.77-μm-diameter disk in Fig. 2(j) is visibly off-center, with a 100 nm offset toward the top-left of AlO_x. The deposition morphology in Fig. 2(j) resembles the eddy structure from boundary-driven flow into a cavity with a depth-to-width ratio of one-third, suggesting that flow over the features is laminar and the resulting deposition shape and cross section can be simulated from flow.[33,34] It may be possible to achieve smaller features by using thinner resist layers or by choosing pattern geometries that intentionally channel the flow, but these approaches will be pattern specific and are beyond the scope of this work.

To explore the utility of this patterning technique for magnonic and magnetoelectric devices, the magnetization dynamics of these microstructures are studied using FMR. Measurements are performed at room temperature in a Bruker EPR spectrometer with the microwave frequency held near 9.83 GHz, while the applied magnetic field is swept across the V[TCNE]$_x$ resonance. Scans are then repeated for multiple polar angles, θ, from out-of-plane (θ = 0°, OOP) to in-plane (θ = 90°, IP) and for multiple azimuthal angles, φ, from parallel to the x-axis (φ = 0°) to perpendicular to the x-axis (φ = 90°).

Figure 3 shows the results of FMR characterization of 1-μm-wide bars aligned parallel to the x-axis and 5-μm-diameter disks. The bars are spaced 20 μm center-to-center in a 1D array, and the disks are spaced 40 μm center-to-center in a 2D square array. The position of the uniform mode of the bars (red) and disks (blue) is tracked as a function of orientation in Figs. 3(b) and 3(c). The bars show a single-peaked resonance that varies from 3550 to 3630 Oe as the structures are rotated from OOP to IP. The secondary peaks to the right of the main peak are from residual V[TCNE]$_x$ thin films that are redeposited during liftoff. The disks reveal a more complicated peak structure, which suggests that standing spin-wave modes are present [Fig. 3(i)] and exhibit a larger field difference between OOP and IP resonances. This difference is evident in Fig. 3(d) where the resonances are tracked through multiple high-symmetry directions, revealing the full anisotropy of these structures. When encapsulated, the resonances in both bar and disk samples retained their overall

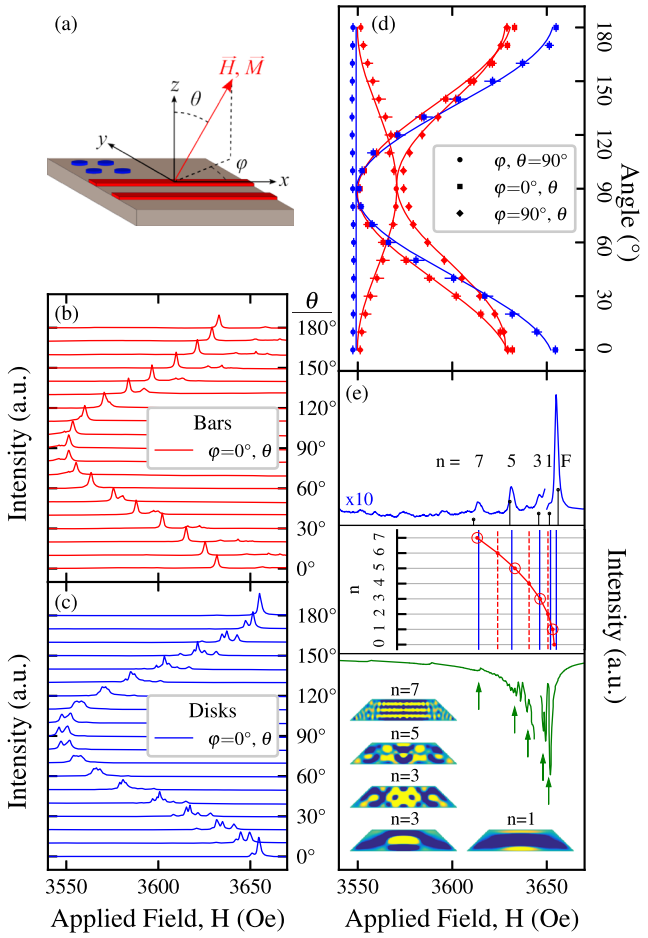

FIG. 3. Ferromagnetic resonance characterization of patterned V[TCNE]$_x$ bars and disks. (a) Schematic of the measurement geometry for the array of 1 μm bars (red) and 5 μm disks (blue) of V[TCNE]$_x$. (b) and (c) FMR response vs applied field for θ = 0° to θ = 180° with φ fixed along the *x*-axis. (d) Uniform mode peak positions (symbols) for three high-symmetry directions and corresponding fit curves [Eq. (3)]. (e) Comparisons of experimental, analytic, and simulated OOP FMR spectra. OOP disk linescan (top, blue) with analytically calculated peak positions (top, black), thickness-mode fitting (middle, red), and micromagnetic simulations (bottom, green) with cross-sectional mode maps (bottom left, yellow and dark blue represent positive and negative motion, respectively, at an instant of time). The thickness-confined mode number predicted from the analytic peaks is shown above the blue OOP linescan. "F" represents the fundamental mode. The solid blue lines in the middle panel indicate experimentally observed odd-mode resonance fields, and the symbols show the best fit field values where the circled points (odd modes) were used for the fits. The red dashed lines show predicted even-mode resonances.

and fine structure for several weeks, indicating similar film lifetimes to encapsulated unpatterned thin films.[24]

The formalism developed by Smit, Beljers, and Suhl[35–37] is used to model this anisotropy. A Cartesian coordinate system is defined with *x* parallel to the length, *y* parallel to the width, and *z* parallel to the thickness of the bars, as shown in Fig. 3(a). By explicitly considering the Zeeman and magnetostatic contributions to the free energy, *F*, one derives the following expression:[38,39]

$$F = -M_i H_i + \frac{1}{2} M_i N_{ij} M_j, \tag{1}$$

where H_i are the components of the applied magnetic field, M_i are the components of the magnetization, and N_{ij} are the components of the demagnetizing tensor, which leads to shape anisotropy, with *i*, *j*, *k* being defined with respect to pattern axes. Solving for harmonic solutions with respect to time and minimizing *F* with respect to θ and φ yields

$$\begin{aligned}\frac{\omega}{\gamma} = \{&[H - 4\pi M_s N_{OP}\cos(2\theta)] \\ &\times [H - 4\pi M_s N_{OP}\cos^2(\theta) - 4\pi M_s N_{IP}\cos(2\varphi)] \\ &- 16\pi^2 M_s^2 N_{IP}^2 \cos^2(\theta)\cos^2(\varphi)\sin^2(\varphi)\}^{1/2},\end{aligned} \tag{2}$$

where

$$N_{OP} \equiv N_z - N_x\cos^2(\varphi) - N_y\sin^2(\varphi), \tag{3a}$$

$$N_{IP} \equiv N_x - N_y, \tag{3b}$$

where N_x, N_y, and N_z are the diagonal components of the demagnetizing tensor, θ is the polar angle, and φ is the azimuthal angle that the sample magnetization makes with the pattern axes [Fig. 3(a)]. Equation (2) is derived assuming that the demagnetizing field is parallel to the magnetization, so $N_{ij} = N_{ij}\delta_{ij} = N_i$, and that the magnetization, (θ_M, φ_M), is parallel to the applied field, (θ_H, φ_H), so only one set of angles is needed to describe the magnetization and applied field, (θ, φ). This approximation is validated by the fact that $4\pi M_s$ for V[TCNE]$_x$ is less than 95 G, and the applied magnetic fields used for these measurements are 3500–3750 Oe. As a result, $\vec{M}$ is parallel to $\vec{H}$ to within 1.5° for the experiments shown here.

The other potential source of anisotropy is the crystal field which arises from the local coordination of the exchange interaction. For uniaxial crystal-field anisotropy, this crystal field can be decomposed into components acting along the pattern axes with the same angular dependence as the demagnetizing anisotropy. As a result, N_i that are extracted from the fit to Eq. (2) are a combination of demagnetizing-field and crystal-field components with the form

$$A_i \equiv N_{i,extracted} = N_{i,demag} + \frac{H_{i,crystal}}{4\pi M_s}, \tag{4}$$

where A_i is the observed anisotropy-tensor component, $N_{i,demag}$ is the geometric demagnetizing-tensor component, and $H_{i,crystal}$ is the additional crystal field along that axis.

Three anisotropy tensors are used to determine the strength of the crystal field in the bars and the disks. The first, $A_{i,fit}$, is generated from simultaneous fits to the three red anisotropy curves in Fig. 3(d) from the bar array to Eq. (2). These fits yield $4\pi M_s$ = 76.57 ± 1.67 G and $|\frac{\gamma}{2\pi}|$ = 2.742 ± 0.040 MHz/Oe, which agree with literature values,[19,21] and $A_{x,fit}$ = 0.00 ± 0.01, $A_{y,fit}$ = 0.189 ± 0.019, and $A_{z,fit}$ = 0.707 ± 0.026. The trace of this anisotropy tensor is 0.896 ± 0.046, indicating that the magnitude of the crystal-field contribution is 7.96 ± 2.47 Oe. Using SEM measurements to geometrically determine a pure demagnetizing tensor for the bars, $N_{i,demag}^{bar}$, that does not include crystal-field effects yields $N_{x,demag}^{bar}$ = 0, $N_{y,demag}^{bar}$ = 0.21, and $N_{z,demag}^{bar}$ = 0.79.[40]

Comparing $A_{i,fit}$ with these $N_{i,demag}^{bar}$, the z and y directions show variation. The easy axis for this uniaxial crystal-field anisotropy will be parallel to the direction of the largest absolute anisotropy, indicating that this crystal field is oriented along the z-axis of the bars. The magnitude of this crystal field is consistent with previous measurements of V[TCNE]$_x$ templated nanowires.[23] In addition to being self-consistent, these results also predict the anisotropy curves for the disks [blue lines in Fig. 3(d)]. To test these fitting results, a final demagnetizing tensor, $N_{i,demag}^{disk}$, for the disk is calculated as $N_{x,demag}^{disk} = N_{y,demag}^{disk} = 0.028$ and $N_{z,demag}^{disk} = 0.944$ based on SEM measurements and demagnetizing expressions from the literature.[41] Combining this with the $4\pi M_s$ and $|\frac{\gamma}{2\pi}|$ values from the previous fit results in the solid blue curves shown in Fig. 3(d) with a combined reduced chi-squared value of 0.96. Adding crystal-field effects degrades the quality of the reduced chi-squared value for $H_{z,crystal}^{disk} > 0.7$ Oe, indicating the absence of crystal-field effects in the disks. These results suggest that the crystal-field contribution arises from anisotropic relaxation in the patterned bars, which corroborates prior work with V[TCNE]$_x$ nanowires where an additional in-plane crystal field is reported due to anisotropy in the relaxation of the templated structures.[23]

The more complicated spectra of the disks suggest that the disks are acting as spin-wave cavities with complex internal mode structure [Fig. 3(e)]. Numerical simulations and analytical calculations are carried out to better understand this mode structure. To begin characterizing the mode structure, the strongest experimental peaks are compared with the odd analytic thickness modes predicted for a thin film in the OOP geometry.[42] The vertical blue lines in Fig. 3(e) represent the experimental peak values. Fitting to these peak values using the mode assignments indicated in Fig. 3(e) and the parameters obtained from the FMR measurements yields the red analytic curve and a value of the exchange stiffness, $A_{ex} = (2.2 \pm 0.5) \times 10^{-10}$ erg/cm. The even thickness modes, shown as dashed red lines, agree well with smaller peaks within the experimental data. Analytic disk calculations shown in black in Fig. 3(e) further describe the identity of the quantum confined modes and agree well when using this A_{ex}. The exchange stiffness depends on M_s; an approximate form, found by several means,[43–45] is $A_{ex} \propto M_s^2$. The exchange length constant $\lambda_{ex} = \frac{2A_{ex}}{\mu_0 M_s^2}$ is therefore a better metric to compare samples with different saturation magnetizations. The difference between the exchange length from this study of $\lambda_{ex} = 9.7$ nm and the previously reported value of 21 nm[21] could be due to differences in the grain structure between the patterned and unpatterned films[45] as well as difficulty in mode assignment, n, in prior work where fewer modes are visible.

Numeric modeling is performed using time-domain micromagnetic simulations with the open-source graphics processing unit-based software MuMax3 while using the material parameters determined from the fits to the experimental data.[46] The factors that have the most relevant influence on the simulated peak structure are (i) the sloped sidewalls that (a) have a strong effect on the shape of the lowest frequency set of peaks which are comprised of a set of closely spaced radially and lowest-order thickness quantized modes and (b) apply an overall shift to the thickness confined modes, (ii) the pinning conditions of the surfaces that have a strong effect on the amplitudes of the thickness-confined modes, and (iii) the exchange stiffness, A_{ex}, that controls the spacing between thickness-confined modes. Sloped sidewalls are used in the simulations to replicate the shape that occurs due to the slower growth rate within 1 μm of the resist. The simulations show that the position of the most prominent peak relative to the thickness-confined modes is sensitive to the exact shape of the sidewalls and the pinning conditions. To account for small differences in the slope of simulated and experimental data, the higher-order thickness modes are aligned with experiment instead of the uniform mode in Fig. 3(e). Simulations with perfect pinning at the top and bottom surfaces agree better with the experimentally observed thickness and radially confined mode structure as compared to simulations with top, bottom, or no pinning; however, the close agreement between the calculated even-mode resonance fields and several smaller peaks in the experimental spectrum suggests that one of the surfaces likely has slightly weaker pinning than the other. Additional simulations can be found in the supplementary material. The resulting simulated frequency response of the simulation is in green in Fig. 3(e) along with several mode maps at peaks indicated by the green arrows. These maps reveal quantization in the thickness and radial directions in the tapered structure. The lower-order thickness modes each show distinct radial quantization. The $n = 7$ thickness mode shows a nearly pure thickness quantization and represents the sum of multiple closely spaced radial modes that are excited simultaneously. The agreement between simulated and experimental spectra demonstrates control over the spin-wave mode structure and lays the foundation for the study and application of magnon cavities with adiabatic boundaries and engineered mode structures.

In addition to analyzing anisotropy and mode structure, FMR can be used to determine the total magnetic loss or damping of these magnon modes. This damping potentially contains both homogeneous and inhomogeneous sources as parameterized via the Gilbert damping factor, α.[47] The damping for the patterned V[TCNE]$_x$ films is measured via broadband ferromagnetic resonance (BFMR) performed in a custom built microstrip-based system wherein the applied magnetic field is held constant in the OOP geometry and the microwave frequency is swept across the V[TCNE]$_x$ resonance. Figure 4 shows the linewidth vs frequency extracted for

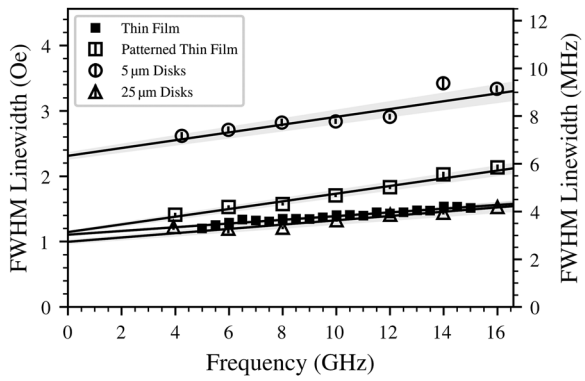

FIG. 4. Full-width at half-maximum linewidth vs resonant frequency for various V[TCNE]$_x$ pattern sizes from thin films to 5-μm-diameter disks. All linewidths are extracted from the OOP geometry. All growths were 1-hour long, resulting in 300-nm-thick 5 μm disks and a 400 nm thickness for the rest. The patterned thin film is a 2 mm by 2 mm patterned patch of V[TCNE]$_x$,

representative samples of disks and unpatterned films, with vertical lines indicating the error in the fits. Representative raw data and fits can be found in the supplemental information. The Gilbert damping is fit using Suhl's expression for the full-width at half-maximum (FWHM) FMR linewidth,[35]

$$\Delta H = \frac{\alpha}{|d\omega_{res}/dH|}\frac{\gamma}{M}\left(F_{\theta\theta} + \frac{1}{\sin^2(\theta)}F_{\varphi\varphi}\right), \quad (5)$$

in combination with phenomenological inhomogeneous broadening.[48] This results in

$$\Delta H = \frac{4\pi\alpha}{|\gamma|}f + \Delta H_0, \quad (6)$$

when one uses $\theta = 0$ for the OOP geometry. The fit frequency linewidths are converted to field linewidths via $\Delta H = \frac{dH}{d\omega}\Delta\omega$, which reduces to $\Delta H = \frac{\Delta\omega}{\gamma}$ for the OOP geometry since $\Delta\omega \ll \omega$.[47,49] In Eq. (6), ΔH is the FWHM linewidth of the resonance, α is the Gilbert damping, and ΔH_0 is the FWHM contribution from inhomogeneous broadening. The fits yield $\alpha = (3.98 \pm 0.22) \times 10^{-5}$ for unpatterned films, $\alpha = (4.60 \pm 0.44) \times 10^{-5}$ for 25 μm disks, and $\alpha = (8.34 \pm 0.77) \times 10^{-5}$ for 5 μm disks. The thin-film damping result of $(3.98 \pm 0.22) \times 10^{-5}$ places V[TCNE]$_x$ films comfortably alongside YIG films as the lowest magnetic damping material currently available, and the retention of that ultralow damping after patterning is considerably better than the reported values for patterned YIG structures.[10–14] In addition to low-damping, the high-frequency measurements of the thin film and 25 μm disks have Quality (Q) factors, $\frac{f}{\Delta f}$, of over 3, 700, competitive with Q factors for YIG thin films.[50] Further examination of the linewidth vs θ and φ in the patterned bars [Fig. 3] reveals the presence of two-magnon scattering processes, indicating that even lower damping and higher Q may be possible with further patterning process refinement.[49] More details can be found in the supplementary material. Retaining ultralow damping and high Q in patterned V[TCNE]$_x$ for features as small as 25 μm and as large as millimeters, both relevant length scales for many magnonic cavity applications,[3,14,51–54] combined with the flexibility to deposit on most inorganic substrates, positions V[TCNE]$_x$ to complement YIG in magnonic and magnetoelectric devices where integration of GGG or high-temperature annealing steps is limiting, such as for small form factors and on-chip integration.

In summary, this work demonstrates a method for patterning the ferrimagnetic coordination compound vanadium tetracyanoethylene. Standard electron-beam lithography of PMMA/P(MMA-MAA) bilayers is used in conjunction with pregrowth aluminum encapsulation and postgrowth dichloromethane liftoff to pattern V[TCNE]$_x$ thin films with no degradation of the microwave magnetic properties. The sidewalls of structures patterned in this way are sloped, allowing for the investigation and quantitative modeling of spin-wave confinement in magnetic structures with soft boundary conditions. Patterned V[TCNE]$_x$ films with features down to 25 μm exhibit a high Q of over 3700 and ultralow damping of $(4.60 \pm 0.44) \times 10^{-5}$, which is competitive with unpatterned YIG and lower than all existing reports of patterned YIG microstructures.[10–14] The versatility of the patterning and deposition conditions of V[TCNE]$_x$, in combination with its ultralow magnetic damping, position V[TCNE]$_x$ as a promising candidate for incorporation into magnetoelectric devices where low-loss, highly coherent magnon excitation is desirable. Such applications range from microwave communications to quantum information.

See the supplementary material for the detailed description of sample fabrication, measurement techniques, simulations, and analytic calculations.

This work was supported by the National Science Foundation Emerging Frontiers in Research and Innovation (NSF-EFRI), Grant No. NSF EFMA-1741666. The authors acknowledge the NanoSystems Laboratory at The Ohio State University.

REFERENCES

[1] Y. Cheng, B. Peng, Z. Hu, Z. Zhou, and M. Liu, "Recent development and status of magnetoelectric materials and devices," Phys. Lett. A **382**, 3018–3025 (2018).
[2] A. Nikitin, A. Ustinov, A. Semenov, A. Chumak, A. Serga, V. I. Vasyuchka, E. Lahderanta, B. Kalinikos, and B. Hillebrands, "Width-modulated magnonic crystal and its application for spin-wave logic," in *2015 European Microwave Conference* (EuMC, 2015).
[3] A. V. Chumak, A. A. Serga, and B. Hillebrands, "Magnonic crystals for data processing," J. Phys. D: Appl. Phys. **50**, 244001 (2017).
[4] H. Chang, P. Li, W. Zhang, T. Liu, A. Hoffmann, L. Deng, and M. Wu, "Nanometer-thick yttrium iron garnet films with extremely low damping," IEEE Magn. Lett. **5**, 1–4 (2014).
[5] C. Hauser, T. Richter, N. Homonnay, C. Eisenschmidt, M. Qaid, H. Deniz, D. Hesse, M. Sawicki, S. G. Ebbinghaus, and G. Schmidt, "Yttrium iron garnet thin films with very low damping obtained by recrystallization of amorphous material," Sci. Rep. **6**, 20827 (2016).
[6] A. A. Serga, A. V. Chumak, and B. Hillebrands, "YIG magnonics," J. Phys. D: Appl. Phys. **43**, 264002 (2010).
[7] T. Schneider, A. A. Serga, B. Leven, B. Hillebrands, R. L. Stamps, and M. P. Kostylev, "Realization of spin-wave logic gates," Appl. Phys. Lett. **92**, 022505 (2008).
[8] O. Zahwe, B. Abdel Samad, B. Sauviac, J. P. Chatelon, M. F. Blanc Mignon, J. J. Rousseau, M. Le Berre, and D. Givord, "Yig thin film used to miniaturize a coplanar junction circulator," J. Electromagn. Waves Appl. **24**, 25–32 (2010).
[9] A. V. Chumak, "Magnon spintronics," in *Spintronics Handbook: Spin Transport and Magnetism*, 2nd ed. (CRC Press, 2019), pp. 247–302.
[10] C. Hahn, V. V. Naletov, G. de Loubens, O. Klein, O. d' Allivy Kelly, A. Anane, R. Bernard, E. Jacquet, P. Bortolotti, V. Cros *et al.*, "Measurement of the intrinsic damping constant in individual nanodisks of $Y_3Fe_5O_{12}$ and $Y_3Fe_5O_{12}$|Pt," Appl. Phys. Lett. **104**, 152410 (2014).
[11] M. B. Jungfleisch, W. Zhang, W. Jiang, H. Chang, J. Sklenar, S. M. Wu, J. E. Pearson, A. Bhattacharya, J. B. Ketterson, M. Wu *et al.*, "Spin waves in micro-structured yttrium iron garnet nanometer-thick films," J. Appl. Phys. **117**, 17D128 (2015).
[12] A. Krysztofik, L. E. Coy, P. Kuświk, K. Załęski, H. Głowiński, and J. Dubowik, "Ultra-low damping in lift-off structured yttrium iron garnet thin films," Appl. Phys. Lett. **111**, 192404 (2017).
[13] S. Li, W. Zhang, J. Ding, J. E. Pearson, V. Novosad, and A. Hoffmann, "Epitaxial patterning of nanometer-thick $Y_3Fe_5O_{12}$ films with low magnetic damping," Nanoscale **8**, 388–394 (2016).
[14] N. Zhu, H. Chang, A. Franson, T. Liu, X. Zhang, E. Johnston-Halperin, M. Wu, and H. X. Tang, "Patterned growth of crystalline $Y_3Fe_5O_{12}$ nanostructures with engineered magnetic shape anisotropy," Appl. Phys. Lett. **110**, 252401 (2017).
[15] M. C. Onbasli, A. Kehlberger, D. H. Kim, G. Jakob, M. Kläui, A. V. Chumak, B. Hillebrands, and C. A. Ross, "Pulsed laser deposition of epitaxial yttrium iron garnet films with low Gilbert damping and bulk-like magnetization," APL Mater. **2**, 106102 (2014).
[16] S. A. Manuilov and A. M. Grishin, "Pulsed laser deposited $Y_3Fe_5O_{12}$ films: Nature of magnetic anisotropy II," J. Appl. Phys. **108**, 013902 (2010).
[17] S. A. Manuilov, R. Fors, S. I. Khartsev, and A. M. Grishin, "Submicron $Y_3Fe_5O_{12}$ film magnetostatic wave band pass filters," J. Appl. Phys. **105**, 033917 (2009).

[18]M. Harberts, Y. Lu, H. Yu, A. J. Epstein, and E. Johnston-Halperin, "Chemical vapor deposition of an organic magnet, vanadium tetracyanoethylene," J. Visualized Exp. **101**, e52891 (2015).
[19]H. Yu, M. Harberts, R. Adur, Y. Lu, P. C. Hammel, E. Johnston-Halperin, and A. J. Epstein, "Ultra-narrow ferromagnetic resonance in organic-based thin films grown via low temperature chemical vapor deposition," Appl. Phys. Lett. **105**, 012407 (2014).
[20]K. Pokhodnya, M. Bonner, V. Prigodin, A. J. Epstein, and J. S. Miller, "Carrier transport in the $V[TCNE]_x$(TCNE = tetracyanoethylene; $x \sim 2$) organic-based magnet," J. Phys.: Condens. Matter **25**, 196001 (2013).
[21]N. Zhu, X. Zhang, I. H. Froning, M. E. Flatté, E. Johnston-Halperin, and H. X. Tang, "Low loss spin wave resonances in organic-based ferrimagnet vanadium tetracyanoethylene thin films," Appl. Phys. Lett. **109**, 082402 (2016).
[22]H. Liu, C. Zhang, H. Malissa, M. Groesbeck, M. Kavand, R. McLaughlin, S. Jamali, J. Hao, D. Sun, R. A. Davidson *et al.*, "Organic-based magnon spintronics," Nat. Mater. **17**, 308–312 (2018).
[23]M. Chilcote, M. Harberts, B. Fuhrmann, K. Lehmann, Y. Lu, A. Franson, H. Yu, N. Zhu, H. Tang, G. Schmidt *et al.*, "Spin-wave confinement and coupling in organic-based magnetic nanostructures," APL Mater. **7**, 111108 (2019).
[24]I. H. Froning, M. Harberts, Y. Lu, H. Yu, A. J. Epstein, and E. Johnston-Halperin, "Thin-film encapsulation of the air-sensitive organic-based ferrimagnet vanadium tetracyanoethylene," Appl. Phys. Lett. **106**, 122403 (2015).
[25]D. Bardoliwalla, "Fast curing, low exotherm epoxy potting and encapsulating systems," in *Proceedings: Electrical Insulation Conference and Electrical Manufacturing and Coil Winding Conference* (IEEE, 1997).
[26]M. S. Thorum, K. I. Pokhodnya, and J. S. Miller, "Solvent enhancement of the magnetic ordering temperature (T_c) of the room temperature $V[TCNE]_x$·S (S = solvent, TCNE = tetracyanoethylene; $x \approx 2$) magnet," Polyhedron **25**, 1927–1930 (2006).
[27]K. I. Pokhodnya, D. Pejakovic, A. J. Epstein, and J. S. Miller, "Effect of solvent on the magnetic properties of the high-temperature $V[TCNE]_x$ molecule-based magnet," Phys. Rev. B **63**, 174408 (2001).
[28]J. Zhang, J. S. Miller, C. Vazquez, P. Zhou, W. B. Brinckerhoff, and A. J. Epstein, "Improved synthesis of the $V(tetracyanoethylene)_x \cdot y$(solvent) room-temperature magnet: Doubling of the magnetization at room temperature," ACS Symp. Ser. **644**, 311–318 (1996).
[29]A. Tseng, K. Chen, C. Chen, and K. Ma, "Electron beam lithography in nanoscale fabrication: Recent development," IEEE Trans. Electron. Packag. Manuf. **26**, 141–149 (2003).
[30]D. Tennant and A. Bleier, "Electron beam lithography of nanostructures," Compr. Nanosci. Technol. **4**, 35–62 (2011).
[31]S. Hu, O. Dyck, H. Chen, Y.-c. Hsiao, B. Hu, G. Duscher, M. Dadmun, and B. Khomami, "The impact of selective solvents on the evolution of structure and function in solvent annealed organic photovoltaics," RSC Adv. **4**, 27931–27938 (2014).
[32]R. Tait, T. Smy, and M. Brett, "Modelling and characterization of columnar growth in evaporated films," Thin Solid Films **226**, 196–201 (1993).
[33]P. N. Shankar and M. D. Deshpande, "Fluid mechanics in the driven cavity," Annu. Rev. Fluid Mech. **32**, 93–136 (2000).
[34]S. Taneda, "Visualization of separating Stokes flows," J. Phys. Soc. Jpn. **46**, 1935–1942 (1979).
[35]H. Suhl, "Ferromagnetic resonance in nickel ferrite between one and two kilomegacycles," Phys. Rev. **97**, 555–557 (1955).
[36]J. Smit and H. G. Beljers, "Ferromagnetic resonance absorption in $BaFe_{12}O_{19}$, a highly anisotropic crystal," Philips Res. Rep. **10**, 113–130 (1955).
[37]L. Baselgia, M. Warden, F. Waldner, S. L. Hutton, J. E. Drumheller, Y. Q. He, P. E. Wigen, and M. Maryško, "Derivation of the resonance frequency from the free energy of ferromagnets," Phys. Rev. B **38**, 2237–2242 (1988).
[38]J. Smit and H. Wijn, "Physical properties of ferrites," Adv. Electron. Electron Phys. **6**, 69–136 (1954).
[39]A. H. Morrish, *The Physical Principles of Magnetism* (IEEE, 2001).
[40]A. Smith, K. K. Nielsen, D. V. Christensen, C. R. H. Bahl, R. Bjørk, and J. Hattel, "The demagnetizing field of a nonuniform rectangular prism," J. Appl. Phys. **107**, 103910 (2010).
[41]L. Kraus, "The demagnetization tensor of a cylinder," Czech J. Phys. **23**, 512–519 (1973).
[42]B. A. Kalinikos and A. N. Slavin, "Theory of dipole-exchange spin wave spectrum for ferromagnetic films with mixed exchange boundary conditions," J. Phys. C: Solid State Phys. **19**, 7013–7033 (1986).
[43]R. Skomski, A. Kashyap, Y. Qiang, and D. J. Sellmyer, "Exchange through nonmagnetic insulating matrix," J. Appl. Phys. **93**, 6477–6479 (2003).
[44]R. Skomski, "Nanomagnetic scaling," J. Magn. Magn. Mater. **272-276**, 1476–1481 (2004).
[45]R. Moreno, R. F. L. Evans, S. Khmelevskyi, M. C. Muñoz, R. W. Chantrell, and O. Chubykalo-Fesenko, "Temperature-dependent exchange stiffness and domain wall width in Co," Phys. Rev. B **94** (2016).
[46]A. Vansteenkiste, J. Leliaert, M. Dvornik, M. Helsen, F. Garcia-Sanchez, and B. Van Waeyenberge, "The design and verification of MuMax3," AIP Adv. **4**, 107133 (2014).
[47]S. S. Kalarickal, P. Krivosik, M. Wu, C. E. Patton, M. L. Schneider, P. Kabos, T. J. Silva, and J. P. Nibarger, "Ferromagnetic resonance linewidth in metallic thin films: Comparison of measurement methods," J. Appl. Phys. **99**, 093909 (2006).
[48]B. Heinrich, J. F. Cochran, and R. Hasegawa, "FMR linebroadening in metals due to two-magnon scattering," J. Appl. Phys. **57**, 3690–3692 (1985).
[49]M. J. Hurben and C. E. Patton, "Theory of two magnon scattering microwave relaxation and ferromagnetic resonance linewidth in magnetic thin films," J. Appl. Phys. **83**, 4344–4365 (1998).
[50]M. Balinskiy, B. Mongolov, D. Gutierrez, H. Chiang, A. Slavin, and A. Khitun, "Perpendicularly magnetized YIG-film resonators and waveguides with high operating power," AIP Adv. **7**, 056612 (2017).
[51]A. V. Chumak, A. A. Serga, and B. Hillebrands, "Magnon transistor for all-magnon data processing," Nat. Commun. **5**, 4700 (2014).
[52]L. Cornelissen, J. Liu, B. van Wees, and R. Duine, "Spin-current-controlled modulation of the magnon spin conductance in a three-terminal magnon transistor," Phys. Rev. Lett. **120**, 097702 (2018).
[53]R. G. E. Morris, A. F. van Loo, S. Kosen, and A. D. Karenowska, "Strong coupling of magnons in a YIG sphere to photons in a planar superconducting resonator in the quantum limit," Sci. Rep. **7**, 11511 (2017).
[54]X. Zhang, C.-L. Zou, L. Jiang, and H. X. Tang, "Strongly coupled magnons and cavity microwave photons," Phys. Rev. Lett. **113**, 156401 (2014).